# Coronal line forest AGN - II. Analysis of the spectral energy distribution

F. C. Cerqueira-Campos [ORCID],[1]★ A. Rodríguez-Ardila,[1,2]★† S. Panda,[2,3]★ R. Riffel [ORCID],[4,5]
L. G. Dahmer-Hahn[2,6] and M. Marinello[2]

[1]*Divisão de Astrofísica, Instituto Nacional de Pesquisas Espaciais, Avenida dos Astronautas 1758, São José dos Campos, 12227-010 SP, Brazil*
[2]*Laboratório Nacional de Astrofísic, Rua dos Estados Unidos 154, Bairro das Nações, CEP 37504-364, Itajubá, MG, Brazil*
[3]*Center for Theoretical Physics, Polish Academy of Sciences, Al. Lotników 32/46, 02-668 Warsaw, Poland*
[4]*Departamento de Astronomia, Instituto de Física, Universidade Federal do Rio Grande do Sul, Av. Bento Gonçalves, 9500, 91509-900 Porto Alegre, RS, Brazil*
[5]*Instituto de Astrofísica de Canarias, Calle Vía Láctea s/n, E-38205 La Laguna, Tenerife, Spain*
[6]*Shanghai Astronomical Observatory, Chinese Academy of Sciences, 80 Nandan road, Shanghai 200030, China*

## ABSTRACT

Coronal-Line Forest Active Galactic Nuclei (CLiF AGN) are characterized by strong, high-ionization lines, which are in contrast to what is found in typical AGNs. Here, we carry out an infrared analysis aimed at understanding the spectral energy distribution (SED) of six sources from this group. In this work, the properties of the dusty torus for these objects are analysed. To this purpose, we infer the physical and geometrical properties of the dust structure that surrounds the central region by fitting with models, the SED of CLiF AGNs in the infrared. For this analysis, we compare the results of three models: CLUMPY, SKIRTOR, and CAT3D-WIND. Using the Bayesian information criterion, SKIRTOR was found to have the most robust fit to the SEDs in five out of six galaxies. The remaining object was best fitted with CLUMPY. The results indicate that these objects are preferentially Type I sources, supporting the detection of broad components in the permitted lines, likely associated with the broad-line region in the near-infrared spectra. The best SED fitting indicates that the line of sight gives access to the view of the central source for these objects, but the amount of dusty clouds in the same direction is high, suggesting the hypothesis that they obscure the emission of the continuum produced by the central source and that the obscuration makes the coronal lines to not overlap with the continuum.

**Key words:** techniques: spectroscopic – galaxies: active – galaxies: Seyfert – infrared: galaxies.

## 1 INTRODUCTION

According to the unified model (Antonucci & Miller 1985), the different spectral characteristics of active galactic nuclei (AGNs) are explained by the relative orientation between the axis of a dusty torus that surrounds the central source and the observer. The bulk of this structure is responsible for absorbing a significant fraction of the optical/ultraviolet continuum produced by the central source, and re-emitting it in infrared (IR) wavelengths. Under this assumption, the diversity of spectral features observed in Type I and Type II AGNs is directly dependent on the line of sight between the central source and the observer. Observational evidence that the unresolved region of the AGNs is surrounded by an obscuring dusty structure abounds in the literature (Tristram et al. 2007; Kishimoto et al. 2011; Hoenig et al. 2012; Burtscher et al. 2013; Hönig et al. 2013, 2014; Tristram et al. 2014; López-Gonzaga et al. 2016; García-Burillo et al. 2019, 2021; Leftley et al. 2021). Moreover, the data suggest that the structure of this obscuring material in some cases is not only associated with

a hot equatorial dust disc, but also with polar dust clouds (Braatz et al. 1993; Cameron et al. 1993; Asmus 2019; Hönig 2019). This polar dust is located on scales from tens to hundreds of parsecs from the central source (Asmus, Hoenig & Gandhi 2016). The works of Müller-Sánchez et al. (2011) and Riffel et al. (2021) indicate that the coronal line region (CLR) is situated on this same scale.

The emission of coronal lines (CLs) in AGNs is mainly associated with the existence of highly energetic processes of the central engine. The study of the emitting region of these lines is important to trace the influence of the AGN in the host galaxy. CLs are not uncommon in AGN spectra, but not all AGNs display them. Riffel, Rodriguez-Ardila & Pastoriza (2006), in a near-infrared (NIR) study of a sample of 47 AGNs, found that in ∼68 per cent of the objects, only one CL is identified (being they the emission lines of [S VIII], [S IX], [Si VI], [Si X], and [Ca VIII]). Overall, in the sources where these lines are detected, they tend to be weak. In the optical regime, the typical values for the log ratio [O III] $\lambda5007$/[Fe VII] $\lambda6087$ is $-0.24 \pm 0.04$ and $-0.44 \pm 0.06$ for Seyfert 1 and Seyfert 2, respectively (Gelbord, Mullaney & Ward 2009). It is important to notice that [Fe VII] $\lambda6087$ is one of the most intense CLs in the optical spectrum.

Rose, Elvis & Tadhunter (2015a), Rose et al. (2015b) and Glidden et al. (2016) introduced in the literature a new class of AGNs dubbed CL Forest AGNs (CLiF AGNs). The optical spectrum of these objects is characterized by a plethora of unusually bright CLs. Rose et al.

★ E-mail: fernando.campos@inpe.br (FCC); aardila@lna.br (ARA); spanda@lna.br (SP)
† Visiting Astronomer at the Infrared Telescope Facility, which is operated by the University of Hawaii under contract NNH14CK55B with the National Aeronautics and Space Administration.

(2015a) claimed that in these particular sources, the CLs are produced in the inner wall of the dusty torus that surrounds the supermassive black hole, with the assumption that at the limit of the radius of dust sublimation, a more refractive dust region is being intensely irradiated, undergoing ablation. According to Krolik & Kriss (1996), under these conditions, thermal winds of highly ionized gas emerge and produce the observed CL forest. If this scenario is correct, in order to detect the CLR in CLiF AGNs, the relative orientation between the inner wall of the torus and the observer is restricted to a short-range of intermediate angles, between that of Type I and II AGNs.

In Cerqueira-Campos et al. (2021, hereafter Paper I), an extensive analysis of CLiF AGNs regarding the optical/NIR continuum emission, their spectral classification, extinction, gas kinematics, and determination of their black hole masses was carried out. The results obtained indicated the presence of broad components in the permitted emission lines in the NIR spectra, allowing to re-classify most CLiFs sources as Type I AGNs. Through comparisons with line ratios and CLs luminosity with other non-CLiF AGNs, it was possible to verify that there are no clear distinctions between CLiF and non-CLiF AGNs. The gas kinematics in CLiFs suggested a compact NLR, of the order of a few arcsecs centred at the central source (<500 pc) (Paper I). The black hole masses for this sample lie in the range between $10^7$–$10^8$ $M_\odot$, supporting the hypothesis that these sources have hotter accretion discs (Panda et al. 2018; Prieto et al. 2022). In the optical region, the luminosities found for CLs in CLiF AGNs are between $10^{40}$–$10^{41}$ erg s$^{-1}$ (Paper I). These values are in the upper range of luminosity reported by Gelbord et al. (2009), in a sample of 63 AGNs. Therefore, although not a separate class of AGNs, CLiFs tend to show extreme values in the properties studied.

The spectral signature of the dusty torus is highly prominent in the IR. Emission from hot dust from the AGN extends beyond 10 to ∼30 $\mu$m (Rieke & Low 1975). However, observational evidence supports models that describe the 1 to 10 $\mu$m continuum as being predominantly or entirely due to hot dust emission, without major influences of the emission from the host galaxy (Edelson & Malkan 1986; Barvainis 1987; Alonso-Herrero et al. 2003; Martínez-Paredes et al. 2017). Therefore, fitting the IR spectral energy distribution (SED) is a good approach to infer the physical properties of the dusty structure around the central source. The analysis of Rieke & Lebofsky (1981), using models generated from large aperture spectra (approximately 8 arcsec), concluded that the emission in the NIR is dominated by thermal radiation produced by hot dust with a temperature between 1300–1500 K. More recently, new models available in the community better reproduce the observed SEDs (Nenkova, Ivezić & Elitzur 2002; Fritz, Franceschini & Hatziminaoglou 2006; Nenkova et al. 2008b; Hönig & Kishimoto 2010; Siebenmorgen, Heymann & Efstathiou 2015; Stalevski et al. 2016; Hönig & Kishimoto 2017).

The torus models so far available in the literature can be divided into three classifications: smooth, clumpy, and two-phase models. Initially, the first models were simpler and had a continuous or smooth distribution of dust in the torus, with a distribution of different radial and vertical density profiles (Pier & Krolik 1992; Granato & Danese 1994; Efstathiou & Rowan-Robinson 1995; Fritz et al. 2006). As dust would hardly survive in the medium with an unique continuous distribution, new models with dust organized into clouds were developed (Nenkova et al. 2002; van Bemmel & Dullemond 2003; Nenkova et al. 2008b; Hönig & Kishimoto 2010, 2017). In addition, two-phase models, which use a scenario with the distribution of dust in both ways together, smooth and clumpy, were

available in the literature (Stalevski et al. 2012; Siebenmorgen et al. 2015; Stalevski et al. 2016).

In Paper I, we verified that CLiF AGNs do not display spectroscopic properties that make them different from the distribution of non-CLiF AGNs. However, the physical mechanisms that produce such prominent CLs are still a matter of debate. Thus, in this second paper, the properties of the dusty torus in these objects are analysed. To this purpose, we derive the physical and geometric properties of the dusty structure, by fitting physically motivated components to recover their SEDs in the IR.

This paper is organized as follows: We detail in Section 2 the sample and observations. In Section 3, we present the SED analysis using the CLUMPY, SKIRTOR, and CAT3D-WIND models (Nenkova et al. 2008b; Stalevski et al. 2016; Hönig & Kishimoto 2017). In order to expand the discussion, we compare our results with those gathered for non-CLiF AGNs in Section 4. Main conclusions are drawn in Section 5.

## 2 SAMPLE, OBSERVATIONS, AND DATA REDUCTION

The sample chosen for this analysis consists of the six CLiF AGNs out of the seven already identified by Rose et al. (2015a), observed using NIR (7800 Å ≤ λ ≤ 25 000 Å) spectroscopy and mid-infrared (MIR) and far-infrared (FIR) photometry. The objects identification are: ESO138-G001, SDSS J164126.91+432121.5, III Zw 77, Mrk 1388, SDSS 2MASX J113111.05+162739, and NGC 424. The main characteristics of this sample can be found in Paper I.

### 2.1 NIR Spectroscopy

The spectra of SDSS J124134.25+442639.2 and SDSS J164126.91+432121.5 were obtained in queue mode with the 8.1 m Gemini North telescope atop Mauna Kea, using the Gemini Near-IR spectrograph (Elias et al. 2006), in the cross-dispersed mode. The spectra of III Zw 77 and Mrk 1388 were obtained at the NASA 3 m IR Telescope Facility, using the SpeX spectrograph (Rayner et al. 2003), in the short cross-dispersed mode (0.7–2.4 $\mu$m). Finally, the spectra of ESO 138-G001 and NGC 424 were obtained using the ARCoIRIS spectrograph, attached to the 4.1 m Blanco Telescope (Schlawin et al. 2014). A more complete description of NIR spectroscopy for our sample is available on Paper I.

### 2.2 Mid and far infrared photometry

We also employed photometric and spectroscopic measurements in the MIR and FIR regions to construct the SED of the CLiF AGN sample, to derive the torus properties. For NGC 424 and ESO138-G001, these points were taken from spectra obtained by the public Spitzer Heritage Archive.[1] data and reduced by SPICE[2] (Spitzer IRS Custom Extraction). The instrument used for the observations was the IRS (InfraRed Spectrograph), equipped with a slit of 168 arcsecs in length by 10.7 arcsecs wide for the spectral range of 14–38 $\mu$m. For the interval 7.4–14.5 $\mu$m, Spitzer employs a slit of 57 × 3.7 arcsecs.

For ESO 138-G001, to minimize the effects of the host galaxy contribution, we adopted a similar method as that used by Lira et al.

---

[1] https://sha.ipac.caltech.edu/applications/Spitzer/SHA/
[2] https://irsa.ipac.caltech.edu/data/SPITZER/docs/dataanalysistools/tools/spice/
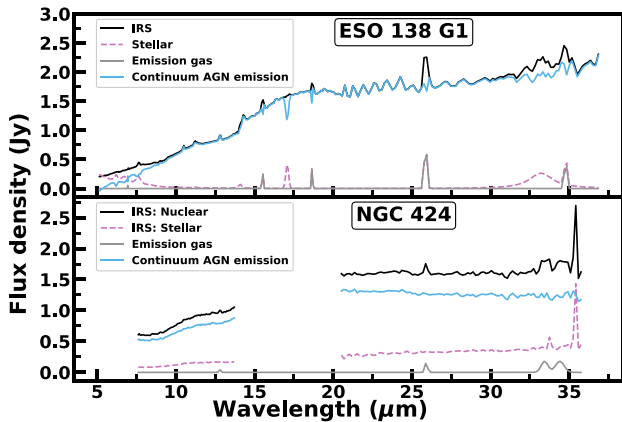
**Figure 1.** Spitzer spectra for ESO 138 G1 and NGC 424. The solid black line represents the nuclear spectrum plus the stellar component, the dashed magenta line represents the stellar component, the solid grey line represents the gas emission, and the solid blue line represents the central source continuum emission.

(2013) and Audibert et al. (2016). It consists of the subtraction of the host galaxy contribution from the observed spectrum of templates developed by Smith et al. (2007), where the MIR light is dominated by the contribution of star-forming regions. In this way, it is possible to obtain a more reliable representation of the spectrum emitted by the AGN. In addition, we removed any potential contribution of star formation using templates and Gaussian representations of other forbidden emission lines. To this purpose we used the PAHFIT tool developed by Smith et al. (2007), made for the low-resolution IRS Spitzer spectra. This software models the observed emission as the sum of the starlight continuum, thermal dust-continuum, pure rotational lines of $H_2$, fine-structure lines, and dust emission features. In our case, as we are interested in isolating the AGN continuum, we decided to subtract only the emission lines from the $H_2$ and the molecular features of PAH (polycyclic aromatic hydrocarbons) emission, stellar contribution and the fine-structure lines.

Most of the emission of PAH lies in the 5–15 $\mu$m interval, where the stellar contribution is most prominent. Unfortunately, for longer wavelengths the separation of stellar emission and AGN continuum is not possible. Thus, this method may overestimate the nuclear emission for $\lambda > 20\,\mu$m. The upper panel of Fig. 1 shows the observed spectrum, the model with the emission PAH and $H_2$ features, and the residual after subtraction of that component.

For NGC 424 we followed a different approach. Because of the large slit width of Spitzer, the spectrum covers not only the AGN but also the host galaxy. For sources with strong nuclear emission such as NGC 424, it was possible to accurately separate both components, thanks to the method employed during the observations. The galaxy was mapped by a set of slits, using one to observe the central region and the host galaxy and another that does not pass through the centre. A more reliable flux density of the central region can be obtained by subtracting the emission with only the galaxy contribution from that with the nuclear and host galaxy components. In addition, we also applied the templates of Smith et al. (2007), to remove the pure rotational lines of $H_2$ and fine-structure lines. It is possible to verify in the bottom panel of Fig. 1, the removal of the NGC 424 host galaxy contribution and nebular emission, resulting in a pure continuum AGN emission.

For 2MASX J113111.05+162739, SDSS J164126.91+432121.5, III Zw 77, and MKR 1388, photometric points were extracted from

the VizieR catalogue data base of the space telescopes *WISE* and *AKARI*.[3] The source of each observation and the fluxes are shown in Table 1.

## 3 SED FITTING

### 3.1 Set of models employed

During the last two decades, several models have been developed to describe the SED of AGNs in the IR, including the signatures that the dusty torus imprints on that distribution. In this work, we used three of these models and compare their results to identify the most likely parameters that best describe the geometry of the dusty torus for each object in the sample.

The first of them is the CLUMPY model (Nenkova et al. 2008a, Nenkova et al. 2008b), which examines the IR emission of the torus, as a function of the inclination angle with respect to the observer. It assumes that the shape of the dusty torus is not homogeneous, but consists of an ensemble of discrete dust clouds. In this scenario, we expect the IR emission at shorter wavelengths to decrease progressively more than the emission at longer wavelengths, as we reach closer to the edge-on orientation. This is due to a combination of an increasing number of clouds intercepted by the line of sight and a higher absorption at the shorter wavelengths, relative to the longer wavelengths.

The CLUMPY models have six free parameters: the number of clouds in the direction of the line of sight ($N_0$); the ratio between the outer and inner radius of the torus ($Y$); the power-law index describing the radial density of clouds of the torus ($q$); the angle between the centre of the system and the outer wall of the torus ($\sigma$); the optical depth ($\tau_\nu$), and the viewing angle of the torus relative to the observer ($i$). The latter parameter is the most relevant one to our work.

The second model is SKIRTOR (Stalevski et al. 2016). It considers the torus to be in a two-phase composition, i.e. the torus geometry consists of a set of high-density dusty clumps immersed in a smooth dusty medium of relatively low density.

The SKIRTOR models have six free parameters. Like CLUMPY, it has the parameters $i$, $Y$, and $\sigma$. In addition, it uses the parameters that represent the edge-on optical depth at 9.7 microns ($\tau_{9.7\,\mu m}$); a power-law index that sets the dust density gradient for the radial ($p$) and polar ($q$) angle. The fraction of total dust mass inside clumps is set to 97 per cent with the remaining 3 per cent for the smooth interclump medium. It does not consider the presence of polar dust clouds.

The third model is CAT3D-WIND (Hönig & Kishimoto 2017). The main feature that differentiates it from CLUMPY is that the former adds a polar outflow, modelled as a hollow cone, which implies a radial distribution of dusty clouds along a polar wind.

The parameters employed to characterize CAT3D-WIND are: The index of the power-law ($q$) that describes the radial dust cloud distribution; the half-opening angle ($\sigma$); the number of clouds along an equatorial line of sight ($N_0$); the index of the dust cloud distribution power-law along the polar wind ($a_w$); the half-opening angle of the wind ($\theta_w$); the angular width of the hollow wind cone ($\sigma_\theta$); the ratio of dust clouds along the line of sight of the wind compared to the one in the disc plane ($f_{wd}$); the outer radius of the torus ($R_{out}$); the

---

[3]This research has made use of the VizieR catalogue access tool, CDS, Strasbourg, France (DOI: 10.26093/cds/vizier). The original description of the VizieR service was published in Ochsenbein, Bauer & Marcout (2000).

**Table 1.** Photometric points in the MIR for the galaxy sample extracted from *WISE* and *AKARI* observations.

| Galaxy | λ (μm) | Flux (mJy) | Origin: filter |
|---|---|---|---|
| **SDSS J164126.90+432121.5** | 22.09 | 48.2 ± 1.6 | *WISE*: W4 |
| | 11.56 | 14.0 ± 0.3 | *WISE*: W3 |
| | 4.60 | 3.7 ± 0.1 | *WISE*: W2 |
| | 3.35 | 2.1 ± 0.1 | *WISE*: W1 |
| **III Zw 77** | 22.09 | 114.0 ± 3.0 | *WISE*: W4 |
| | 11.56 | 49.8 ± 0.7 | *WISE*: W3 |
| | 4.60 | 17.4 ± 0.3 | *WISE*: W2 |
| | 3.35 | 12.3 ± 0.2 | *WISE*: W1 |
| **Mrk 1388** | 22.09 | 228.0 ± 4.0 | *WISE*: W4 |
| | 18.39 | 122.0 ± 52.0 | *AKARI*: L18W |
| | 11.56 | 89.8 ± 1.2 | *WISE*: W3 |
| | 8.61 | 55.8 ± 9.3 | *AKARI*: S9W |
| | 4.60 | 22.8 ± 0.4 | *WISE*: W2 |
| | 3.35 | 14.5 ± 0.3 | *WISE*: W1 |
| **2MASX J113111.05+162739** | 22.09 | 40.5 ± 1.8 | *WISE*: W4 |
| | 11.56 | 19.4 ± 0.3 | *WISE*: W3 |
| | 4.60 | 6.1 ± 0.1 | *WISE*: W2 |
| | 3.35 | 3.3 ± 0.1 | *WISE*: W1 |

optical depth of the individual clouds ($\tau$), and the viewing angle of the torus relative to the observer (*i*).

In order to build the SED for each object of the sample in the MIR and FIR, Spitzer spectra, *WISE*, and *AKARI* photometric points were employed. For the NIR and optical regions, integrated spectra were used. The spectral data source information is described in Section 2. Additional information on the spectroscopy in the NIR is provided in Paper I. The emission lines of the spectra were removed for the fit, so that we only employed the continuum emission.

Since different wavelength ranges are dominated by different components, we first fitted the optical range in order to propagate this component to the remaining regions. This choice was done based on the fact that the optical continuum is expected to be simpler, being composed of a combination of stellar populations, plus a featureless continuum (FC) produced by the AGN. In order to determine the different contributions to the observed continuum in the optical/NIR for our sample (i.e. stellar population and AGN), we have employed the STARLIGHT code (Cid Fernandes et al. 2004, 2005). Basically, the code fits an empirical stellar library to the observed spectrum by minimizing the $\chi^2$, taking into account factors like stellar kinematics and dust reddening.

We fed STARLIGHT with a modified version of the Bruzual & Charlot (2003) library of simple stellar populations, with Chabrier (2003) IMF and Padova (Girardi et al. 2000) isochrones. We have limited the library to the 25 most representative ages[4] and most representative metallicities.[5] We chose this library because it has a very wide wavelength coverage, encompassing most wavelengths analysed in this paper. In order to represent the contribution from the AGN, we added a power law following the expression $f_\lambda \propto \lambda^{-0.5}$. An example of the application of the code and method to the optical and NIR can be found in Dahmer-Hahn et al. (2019). We used the stellar component added to the models mentioned above to build the SED. We then created a NIR + MIR stellar and AGN continuum by fixing the stellar populations and FC fractions derived from the optical, and propagating this continuum to the remaining wavelength ranges.

[4]0.00100, 0.00316, 0.00501, 0.00661, 0.00871, 0.0100, 0.0144, 0.0251, 0.0400, 0.0550, 0.101, 0.161, 0.286, 0.509, 0.904, 1.27, 1.43, 2.50, 4.25, 6.25, 7.50, 10.0, 13.0, 15.0, and 18.0 Gyr
[5]Z = 0.00010, 0.00040, 0.00400, 0.00800, 0.02000, and 0.05000

After determining the best stellar template and the fraction that it contributes in each galaxy, we employed the PYTHON package LMFIT to fit the SED (Newville et al. 2016). LMFIT provides a high-level interface to non-linear optimization and curve-fitting problems. Using this routine, it was possible to identify the best model with respect to the points obtained through observations.

We also employed, for comparison purposes, photometric points for NGC 4151 and NGC 1068 as representatives of Type I and II AGN, respectively. The VizieR photometry tool[3] was used to gather the data. For NGC 1068 in the optical range, a spectrum of the inner $500 \times 500$ pc obtained from the Multi-Unit Spectroscopic Explorer (MUSE) processed archival data was used and the stellar continuum was estimated using the STARLIGHT. The contribution of the stellar population in NGC 4151 is estimated at 15 per cent in the NIR spectrum (Riffel, Storchi-Bergmann & McGregor 2009), therefore the same stellar population template of NGC 1068 was used but normalized to represent 15 per cent of the flux in the NIR for this galaxy SED.

### 3.2 Criterion to choose the best fit

The CLUMPY, SKIRTOR, and CAT3D-WIND models consist of 1.247.400, 19.200, and 124.740 SED templates, respectively. They are constructed through different combinations of the parameters described in Section 3.1.

To build the SED of the objects in our sample, we used the method described in Section 3.1. Moreover, we developed an algorithm in PYTHON to fit the SEDs using the LMFIT package (Newville et al. 2016). It uses a normalization factor for each template in order to obtain the best fit for the observational data. For each fit, the code returns a Bayesian information criterion (BIC) list, with the best fits having the lowest BIC. However, because the solution from the models is intrinsically degenerate, it is necessary to take into account not only the smallest BIC to obtain more realistic results, but also to choose a sample of best fits that do not drastically oppose the best result.

Thus, the final result for each source is the average of the best models that fit the observational data. In this process, we followed the procedure described by Kass & Raftery (1995). Since the best model is the one that provides the minimum BIC, which we will
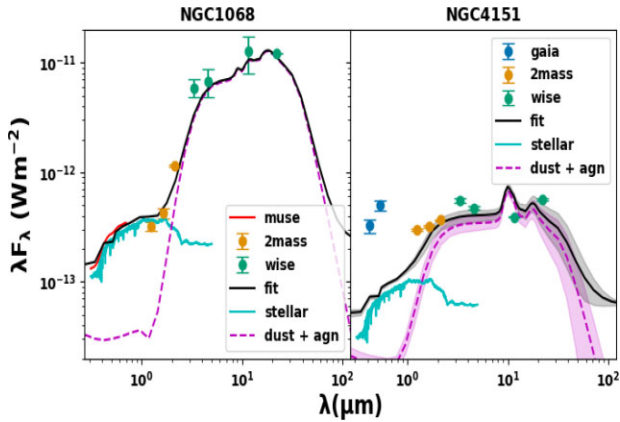
**Figure 2.** Best fit from CLUMPY models to the archetypal Seyfert 1 and 2 galaxies NGC 4151 (right-hand panel) and NGC 1068 (left-hand panel), respectively. The black line represents the fitted SED. The points represent the observational data from *Gaia* (blue), 2MASS (yellow), and *WISE* (green), the red line represents the MUSE data. The shaded area represents the dispersion in the fitted SED.
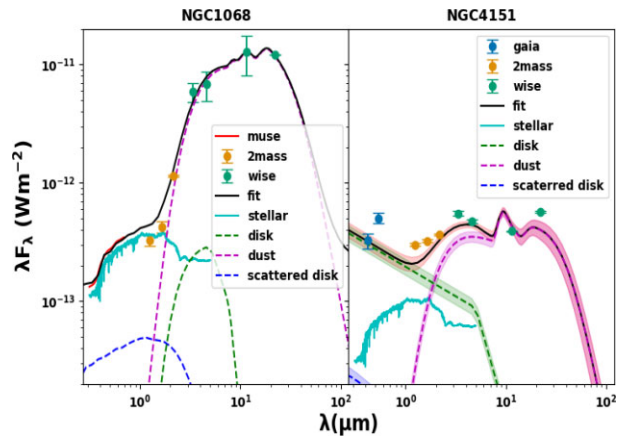


**Figure 3.** Same as Fig. 2, but for the SKIRTOR model.



**Figure 4.** Same as Fig. 2, but for the CAT3D-WIND model.



**Figure 5.** Histogram of the best value for the *i* and $\sigma$ parameters for CLUMPY in the archetypal Seyfert 1 NGC 4151. The orange-dashed line represents the most probable value. The orange solid line is the distribution function, and the vertical orange area the dispersion in the respective value.

denote by BIC∗, the variation $\Delta\mathrm{BIC} = \mathrm{BIC_m} - \mathrm{BIC}*$ is an indicator of opposition to the best model and m being the number of models. With $\Delta\mathrm{BIC} < 6$, the model with the best result presents a positive but not a strong opposition. Thus, we selected the set of models that confronts the smallest model, with a variation of less than six to compose the average SED model.

### 3.3 Test case with NGC 4151 and NGC 1068

In order to test the fitting procedure with CLUMPY, CAT3D-WIND, and SKIRTOR, we first fit the SED of the archetypal Seyfert 1 and 2 galaxies NGC 4151 and NGC 1068, respectively. To compose the SED, photometric points in the optical, NIR, and MIR were extracted from *Gaia*, 2MASS, and *WISE*, respectively, through the VizieR photometry tool.

The best SED fitting obtained for NGC 4151 and NGC 1068 are illustrated in Fig. 2 for CLUMPY, Fig. 3 for SKIRTOR, and in Fig. 4 for CAT3D-WIND. In order to evaluate the consistency of the results in relation to the spectral type, the parameters $\sigma$ and *i* were analysed. For NGC 4151, as only photometric points were used, the problem becomes more degenerate and a group of templates fit in the same model present some opposition with respect to $\Delta\mathrm{BIC}$.
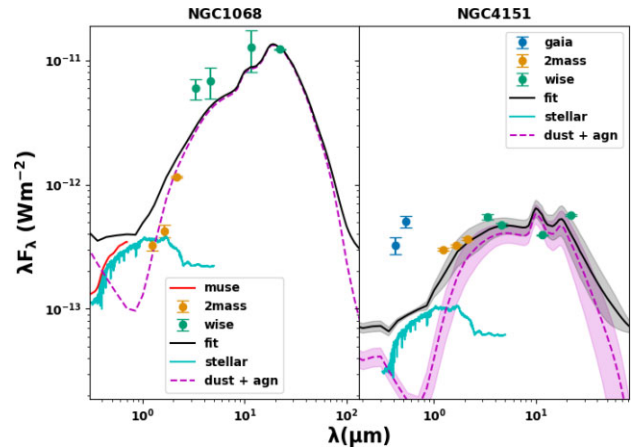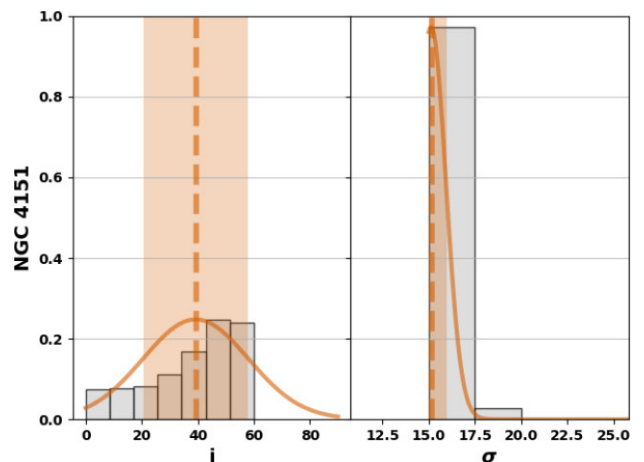
In order to find the most probable value and the uncertainty for each parameter, it was necessary to identify the best function that describes the data sample distribution of each variable. To this purpose, the python package FITTER was used (Cokelaer et al. 2021). It allows the determination of the most probable distribution and the best value of each parameter. We used the lower BIC as a selection criterion among a range of distribution functions (Norm, Rayleigh, Cauchy, Power Norm, $\chi^2$, Power Lognormal, t-distribution, F-distribution, and Weibull Max).

In Figs 5, 6, and 7, we plot the distribution of values of the inclination angle and sigma found using CLUMPY, SKIRTOR, and CAT3D-WIND, respectively, for NGC 4151. In each panel, we show the histogram of the distribution of the parameter values of the models that fulfilled the $\Delta\mathrm{BIC}$ selection criterion. The solid orange line represents the function that describes the best distribution, the vertical orange dashed line represents the most probable value and the orange shaded area is the uncertainty range with $1\sigma$ confidence.

For NGC 4151 the BIC value of the best-fitting template was −544, −530, and −527, for SKIRTOR, CLUMPY, and CAT3D-WIND, respectively. It is not possible to claim that the results are comparable. For the parameter *i*, the values obtained are $18 \pm 13$ using SKIRTOR, $39 \pm 19$ for CLUMPY, and $30 \pm 24$ for CAT3D-WIND. The SKIRTOR
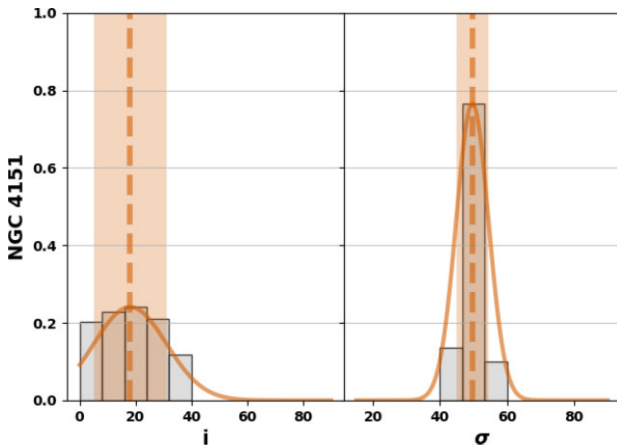
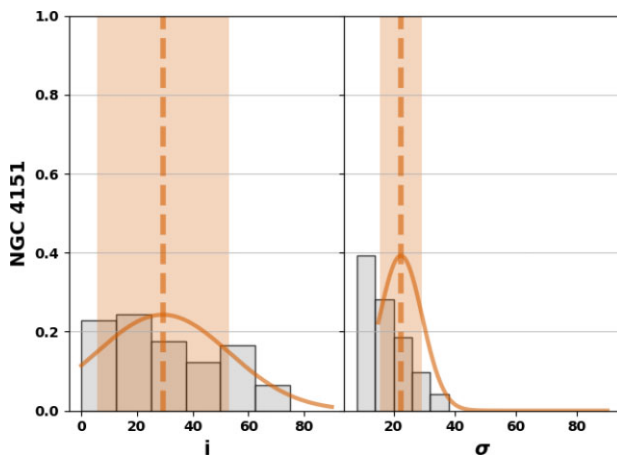**Figure 6.** Same as Fig. 5, but for SKIRTOR.



**Figure 7.** Same as Fig. 5, but for CAT3D-WIND.

value for the viewing angle is compatible, within uncertainties, to $9^{+18}_{-9}°$, reported by Nandra et al. (1997), using X-ray observations from *ASCA*.

For NGC 1068, the BIC value of the best-fitting template was $-120624$, $-121683$, and $-114423$ for SKIRTOR, CLUMPY, and CAT3D-WIND, respectively. For the inclination angle *i*, we found $70 \pm 10°$ for SKIRTOR and $50 \pm 10°$ for CLUMPY. The latter value, despite not having the lowest BIC, is in agreement within uncertainties, with those derived in the literature. García-Burillo et al. (2016), for example, inferred an inclination of $66^{+9}_{-4}°$. Lopez-Rodriguez et al. (2018) found a value of $75^{+8}_{-4}°$ and Gravity Collaboration (2020) derived a value of $70 \pm 5°$. For the *i* identified using CAT3D-WIND, the model has the worst fit among the three models, as the value of $15 \pm 15$ predicted is not consistent with the Type II nature of that source.

It is possible to verify that even employing photometric points from the optical to the MIR spectral windows, the results obtained with the SKIRTOR models are compatible with those in the literature. The outcome of CAT3D-WIND is the least plausible among the three models, not representing the optical region very well in the two test objects. Moreover, regarding the spectral type, the models SKIRTOR and CLUMPY present consistent results, except for the fit with CLUMPY for the NGC 4151, which fails at reproducing the optical part of the SED. Fig. 8 displays a planar diagram with the parameters *i* and $\sigma$,

found using the three SED models. For NGC 1068, both SKIRTOR and CLUMPY, suggest that we are looking at this source through the torus. For NGC 4151, CLUMPY, SKIRTOR, and CAT3D-WIND suggest a viewing angle such that the observer is facing the central source.

### 3.4 SED fitting of CLiF AGNs

After testing the consistency of our approach with two of the most *bonafide* AGNs in the literature, we proceed to the fitting of the CLiF sample. Among the three torus models (i.e. CLUMPY, SKIRTOR, and CAT3D-WIND), to select the one that best describes each object in our sample, the lowest BIC value was used as a criterion. However, if there was a $\Delta$BIC < 6 in the comparison of the BIC results, more than one model will be considered.

In the fitting process, the contribution of the stellar population templates generated by STARLIGHT in the optical region (i.e, at 5400 Å) was set to the values predicted by the stellar synthesis: 75 per cent, 97 per cent, 56 per cent, 75 per cent, 95 per cent, and 67 per cent for ESO 138 G1, SDSS J164+43, III ZW 77, Mrk 1388, 2MASX J113+16, and NGC 424, respectively. Overall, it ranges from 56 to 97 per cent.

Table 2 shows the results of the lowest BIC for each model. When comparing among the three Torus models, there was no solution with $\Delta$BIC < 6. Five objects had the best result with SKIRTOR, one with CLUMPY and none with CAT3D-WIND, suggesting that the polar wind component in these sources is not a prominent contributor to the overall SED. For this reason, the latter was not considered in the analysis that follows. The templates that fit with the lowest BIC value, compared to the second-best fit of the same model, also had a $\Delta$BIC value greater than six. Therefore, only the best-fitting template for each model was considered in the final results. For this reason, the error bars were estimated taking into account the binning of the parameters in the template models.

Figs 9, 10, and 11 show the result of the SED fitting to our galaxy sample. The observational data described in Section 2 is labelled in the figure. The dashed light blue line represents the stellar component, the dashed magenta line represents the dust emission, the dashed dark blue line is the scattered disc component, and the red solid line is the best fit. Tables 3 and 4 list the values of the parameters found for the best fit for each of these two approaches. Fig. 12 displays a planar diagram with the parameters *i* and $\sigma$, found to the best-fitting SED models for CLiF AGNs. For this figure fits made with CLUMPY the grey area represents the parameter $\sigma$, fits made with SKIRTOR, the representation of $\sigma$ is in purple. In all panels of the Fig. 12, the parameter *i* is represented by a black dashed line.

A close inspection of the SED shapes in Figs 3 and 4 obtained for NGC 1068 and NGC 4151, respectively, with the best-fitting SED shapes of the CLiF AGNs (blue panels in Figs 9 and 10) suggests that all but 2MASX J113+16 and NGC 424 have a SED that is very close to that of NGC 4151, this latter object assumed as representative of Type I AGN. It is important to notice, that this latter SEDs is characterized by a flatter shape than that of a Type II AGN. It also shows the presence of silicate emission except in SDSS J164+43, where it is in absorption as suggested by SKIRTOR model (Fig. 10).

Tables 3 and 4 show that the torus inclination determined by CLUMPY and SKIRTOR covers the range of values from 0 to 50°. Overall, the IR emission is compatible with that of a Type I AGN in most objects of the sample.
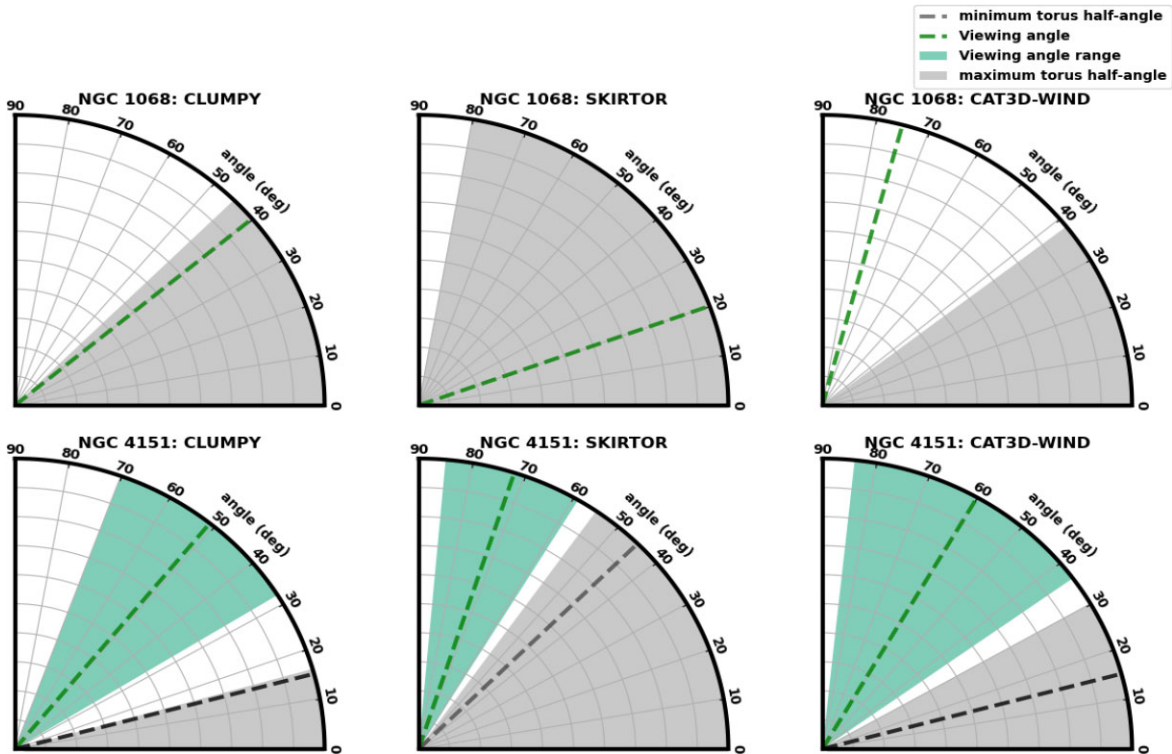
**Figure 8.** The representation of the $\sigma$ and $i$ parameters for the SKIRTOR and CLUMPY models to the galaxies NGC 1068 and NGC 4151. The dashed green line represents the best-fitting value for the viewing angle, and the green area marks the error in the estimation of the viewing angle. The grey area marks the maximum range of the half-opening angle of the torus and the dashed grey line represents the minimum value of the half-opening angle of the torus. In this representation the angle is $0^\circ$, which represents the torus equatorial plane.

**Table 2.** The lowest BIC results for each of the three models in the SED fitting. Values in blue are the best results, while those in red the worst.

| Galaxy | CLUMPY | SKIRTOR | CAT3D-WIND |
|---|---|---|---|
| ESO 138 G1 | **−792636** | −779617 | −781789 |
| SDSS J164+43 | −656610 | **−690268** | −685362 |
| III ZW 77 | −671932 | **−672257** | −653336 |
| Mrk 1388 | −739757 | **−761091** | −744685 |
| 2MASX J113+16 | −660216 | **−697847** | −688366 |
| NGC 424 | −688501 | **−733837** | −731986 |

## 4 COMPARISON OF MODEL PARAMETERS BETWEEN CLIF AND NON-CLIF AGNS

González-Martín et al. (2019, hereafter GM19) carried out an IR SED fitting of 110 AGNs using the Spitzer/IRS spectroscopic data with six different models, including SKIRTOR and CLUMPY. As their sample is fully dominated by non-CLiF AGNs and contains a significant number of objects, it is worth comparing their results with ours. The distribution of the parameter space found for SKIRTOR and CLUMPY in GM19 are illustrated in their figures 15 and 18. The main results of the comparison between each parameter using the GM19 as a reference, can be summarized as follows:

(i) The viewing angle, $i$: The five objects best fitted in this work with SKIRTOR display torus inclination angle $i$ between 10 and $50^\circ$. In the GM19 distribution, the least frequent values of $i$ are 20 and $30^\circ$, which are the values obtained for SDSS J164+43 and III ZW 77, respectively. Moreover, the AGN that is best-fitting with CLUMPY (ESO 138 G1), has an $i$-value of $0^\circ$. It is located in the second largest peak of the distribution in GM19.

(ii) The number of dusty clouds in the direction of the line of sight, $N_0$: In the only AGN that was fit with CLUMPY (ESO 138 G1) the value of $N_0 = 14$ is close to the highest peak of the GM19 distribution.

(iii) The ratio between the outer and inner radius of the torus, ($Y$): The values of 10 and 30 obtained here with SKIRTOR coincide with the two peaks of the distribution in GM19. In SDSS J164+43 and III ZW 77, the $Y$ of 10 and 30, respectively, is not present in their distribution. In ESO 138 G1 (CLUMPY), the $Y$ value of 30 is present in a secondart peak, however not very frequent.

(iv) The radial density of clouds of the torus, $q$ (CLUMPY), and $p$ (SKIRTOR): The value of 0.1 and 1.5 found using SKIRTOR coincides with the peaks of the distribution of GM19, with the value 1.5 being within the largest peak of the distribution. For the one AGN fit with CLUMPY, the value of 0.5 is very frequent.

(v) The half-opening angle, $\sigma$: The results from SKIRTOR provided values of 50, 70, and $80^\circ$, coinciding with peaks in the distribution in GM19. Moreover, the distribution of values of $\sigma$ obtained with CLUMPY in GM19 is quite homogeneous, with a peak at $70^\circ$. The value of $50^\circ$ obtained for ESO 138 G1 does not correspond to any of the peaks in the GM19 distribution.

(vi) The index of the dust density gradient with polar angle function, $q$: In half the sample, the values of $q$ derived from SKIRTOR coincide with peaks of the distribution, shown in GM19. In the remaining objects, $q$ are out of the peaks, but still are within the range of possible values displayed by non-CLiF AGN.

(vii) The edge-on optical depth at 9.7 microns, $\tau_{9.7\mu m}$: The values of 5, 5, and 7 found for III ZW 77, Mrk 1388 and 2MASX J113+16, respectively, coincide with the peaks of the distribution in GM19.
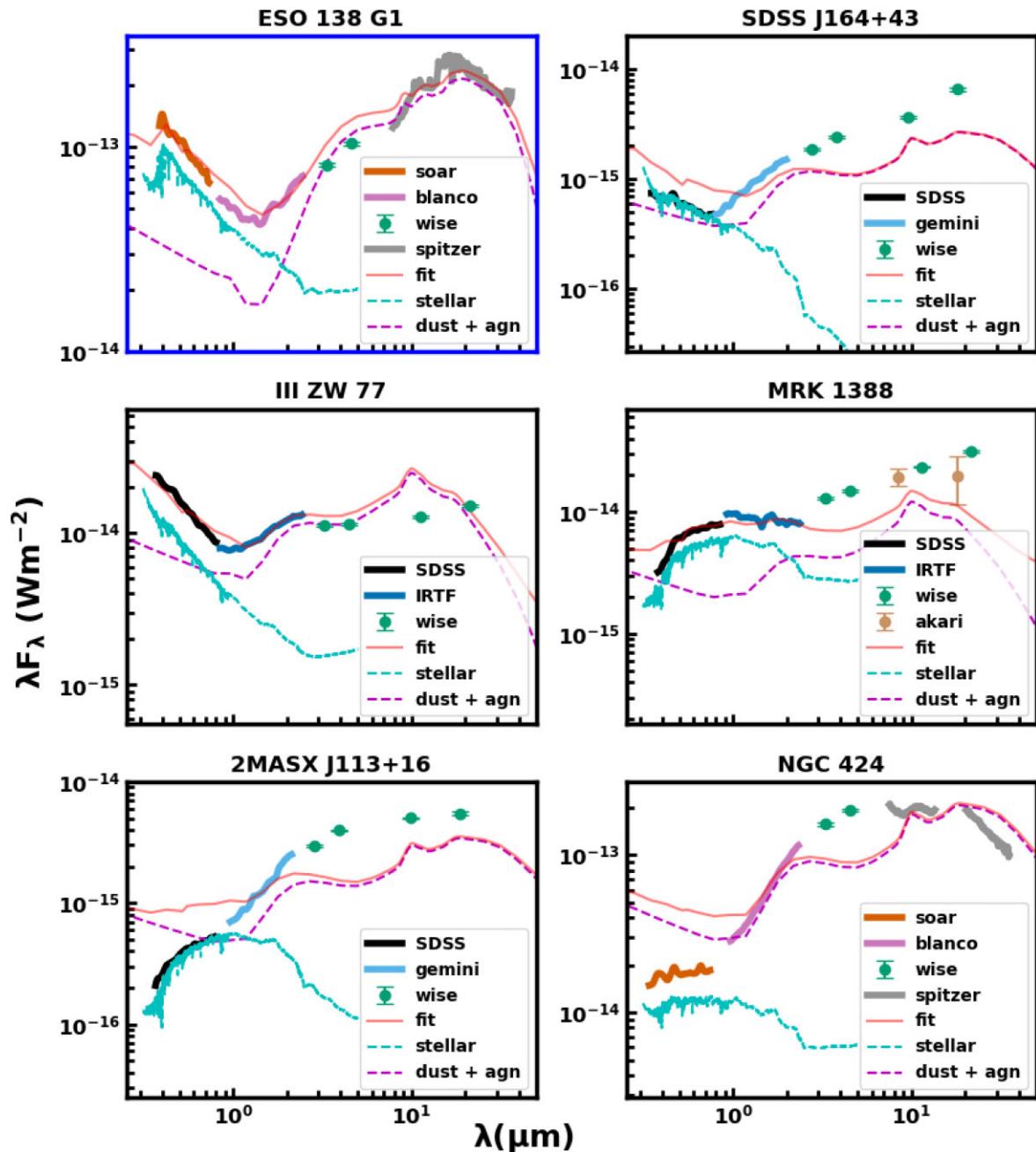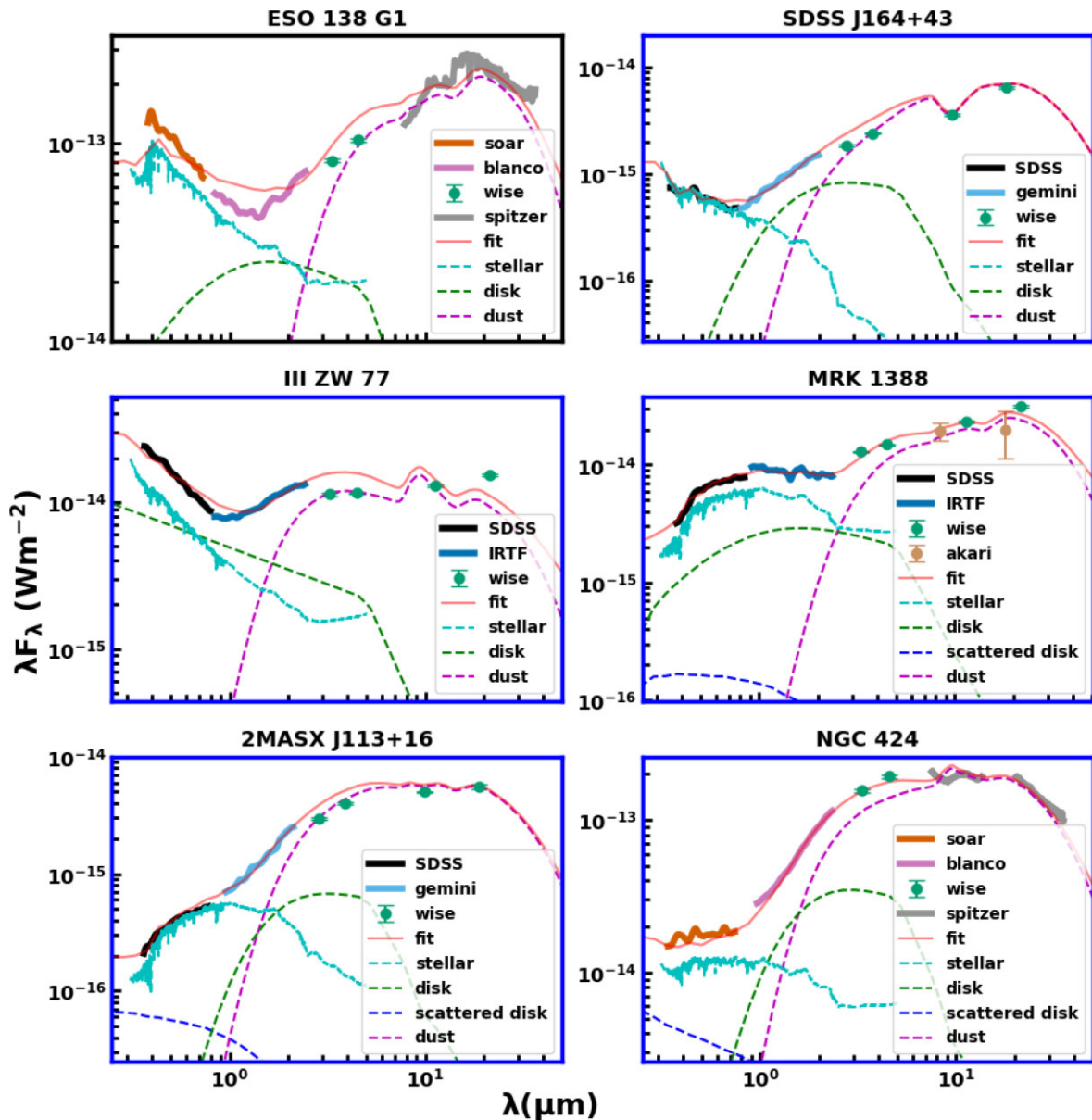
**Figure 9.** Best fit to CLiF AGN SEDs to CLUMPY models. The cyan line represents the stellar component, the dashed magenta line represents the dust plus the central source emission, and the red solid line is the best fit. The panel in blue represents the best fit among all other models. The *x*-axis represents the rest wavelength.

However the value of 9 present in SDSS J164+43 and NGC 424 is less frequent.

(viii) The optical depth of the individual clouds ($\tau$): For ESO 138 G1 (CLUMPY), the value of 20 is frequent in the distribution of GM19.

In summary, for the set of parameters that characterize the SED fitting in CLUMPY and SKIRTOR, the CLiF AGNs do not display values that stand out from the distribution of non-CLiF AGNs. With the exception of some parameters that differ from the distribution of non-clif AGNs (indicated in bold in Table 4), but do not have a

distinct relationship in the sample as a whole. It means that the objects of our sample do not represent a class with very different characteristics from other types of AGNs, regarding the parameters of dusty torus models.

In Paper I, it was found that the physical properties of the emission line gas in CLiF AGNs do not differ from those of non-CLiF AGNs, meaning that the former is not a separate group of AGN. Moreover, it was stated that a specific viewing angle does not define the presence of a strong CL forest. They also found that CLiF AGNs are dominated by Type I objects, and that the black hole mass of the AGN is $<10^8$ M$_\odot$. Finally, the study of their kinematics suggests a compact NLR. In this work, by means of the SED fitting in the optical/IR, we confirm

**Figure 10.** Best fit to CLiF AGN SEDs to SKIRTOR models. The cyan line represents the stellar component, the dashed magenta line represents the dust, the green dashed line represents the central source emission, the dashed blue line represents the scattered disc emission, and the red solid line is the best fit. The panel in blue represents the best fit among all other models. The *x*-axis represents the rest wavelength.

that in CLiF AGN, the line of sight of the observer is directed towards the central engine (see Fig. 12).

It is possible to notice, by looking at Fig. 12, that Mrk 1388 is the only object fit with SKIRTOR where the line of sight to the central engine is intercepted by the bulk of the torus. This result contrasts to what was verified in Paper I. It displays a broad component (full width at half-maximum of 1040 km s$^{-1}$) in the Balmer lines, while Doi (2015) observed a strong FC in the optical spectrum. This would tentatively classify it as a narrow line Seyfert 1 (NLS1). However, a similar broad component is also detected (in blue-shift) in the [O III] lines, which suggests the presence of an outflow rather than a genuine broad-line region (BLR) emission line. In the NIR, broad components were not identified in the lines of H I. The results obtained in this work suggest that Mrk 1388 is a Type II AGN.

For ESO 138 G1, the viewing angle points out that we are looking directly to the central engine. However, the number of clouds in the line of sight is high ($N_0 = 14 \pm 1$). This would heavily obscure the central source, explaining its Type II-type appearance. In SDSS J164+43, 2MASX J113+16, and NGC 424 the results suggest a viewing angle that is grazing the torus, allowing the view of the central source. Likewise, in III Zw 77 the viewing angle allows a direct view to the central source, in agreement with the detection of a truly BLR. These results indicate that although we have a direct view to the central region, the inclination angle points to regions influenced by dust. This then allows a scenario of dust grains being destroyed, favouring the observation of a greater number of CLs. It is also in line with the fact that some CLiF AGN has a hidden BLR in the optical region (Paper I). We are aware of the small number
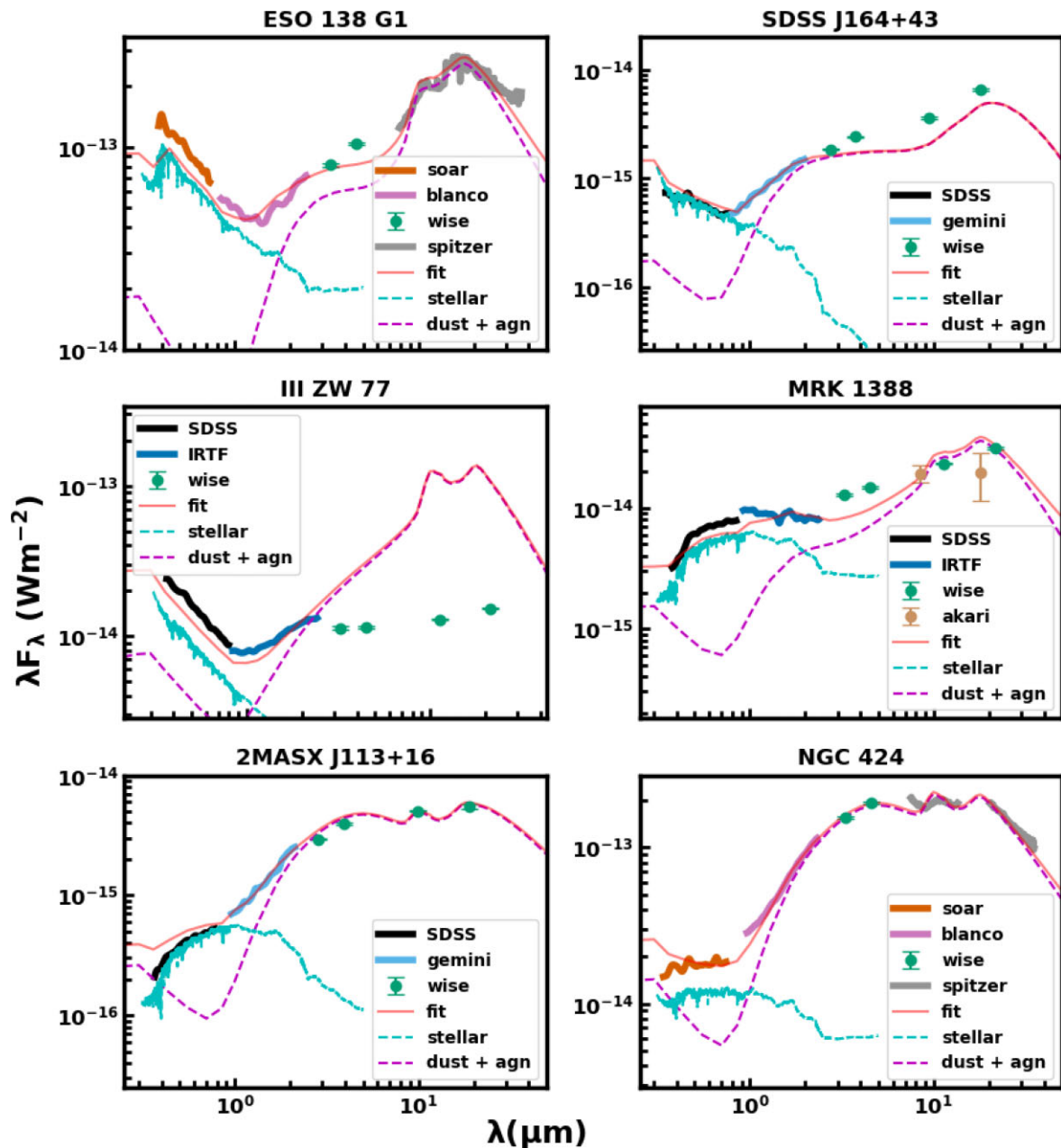
**Figure 11.** Best fit to CLiF AGN SEDs to CAT3D-WIND models. The cyan line represents the stellar component, the dashed magenta line represents the dust plus the central source emission, and the red solid line is the best fit. The *x*-axis represents the rest wavelength.

**Table 3.** Values of the parameters for the galaxy which obtained the best fit with the CLUMPY model.

| Galaxy | $N_0$ | Y | q | $\sigma$ (°) | $\tau_\nu$ | $i$ (°) |
|---|---|---|---|---|---|---|
| ESO 138 G1 | $14 \pm 1$ | $30 \pm 10$ | $0.5 \pm 0.5$ | $50 \pm 5$ | $20^{+20}_{-10}$ | $0^{+10}_{-0}$ |

of of sources currently identified as CLiF AGN, and this may affect these results somehow.

To draw more robust conclusions about the nature of the NLR in objects with CL forests, it is necessary to identify more CLiF AGN and expand the current analysis to them. The analysis carried out so far in this work, as well as in Paper I, shows that the presence of a CL forest is not related to either a special viewing angle or a very exotic property of the emission gas.

## 5 FINAL REMARKS

In this work, we carry out optical plus IR SED fitting in a sample of six galaxies classified as CLiF AGN, using three different torus models, namely CLUMPY, SKIRTOR, and CAT-3D. This approach allowed us to determine the orientation angle of the torus with respect to the observer for all objects. The results show that the viewing angle is compatible with the orientation of a Type I AGN, with the exception of one source (Mrk 1388). We also found from the SED fitting the

**Table 4.** Values of the parameters for each galaxy which obtained the best fit with the SKIRTOR model.

| Galaxy | $i$ (°) | $\tau_{9.7\mu m}$ | $\sigma$ (°) | $p$ | $q$ | $Y$ |
|---|---|---|---|---|---|---|
| SDSS J164+43 | $10 \pm 10$ | $\mathbf{9 \pm 2}$ | $80 \pm 10$ | $1.0 \pm 0.5$ | $0.0^{+0.5}_{-0.0}$ | $\mathbf{20^{+10}_{-10}}$ |
| III ZW 77 | $\mathbf{30 \pm 10}$ | $5 \pm 2$ | $50 \pm 10$ | $1.0 \pm 0.5$ | $0.0^{+0.5}_{-0.0}$ | $\mathbf{20^{+10}_{-10}}$ |
| Mrk 1388 | $50 \pm 10$ | $5 \pm 2$ | $70 \pm 10$ | $0.0^{+0.5}_{-0.0}$ | $1.5^{+0}_{-0.5}$ | $30^{+0}_{-10}$ |
| 2MASX J113+16 | $\mathbf{20 \pm 10}$ | $7 \pm 2$ | $70 \pm 10$ | $1.5^{+0}_{-0.5}$ | $\mathbf{0.5 \pm 0.5}$ | $30^{+0}_{-10}$ |
| NGC 424 | $40 \pm 10$ | $\mathbf{9 \pm 2}$ | $50 \pm 10$ | $0.0^{+0.5}_{-0.0}$ | $\mathbf{0.5 \pm 0.5}$ | $10^{+10}_{-0}$ |
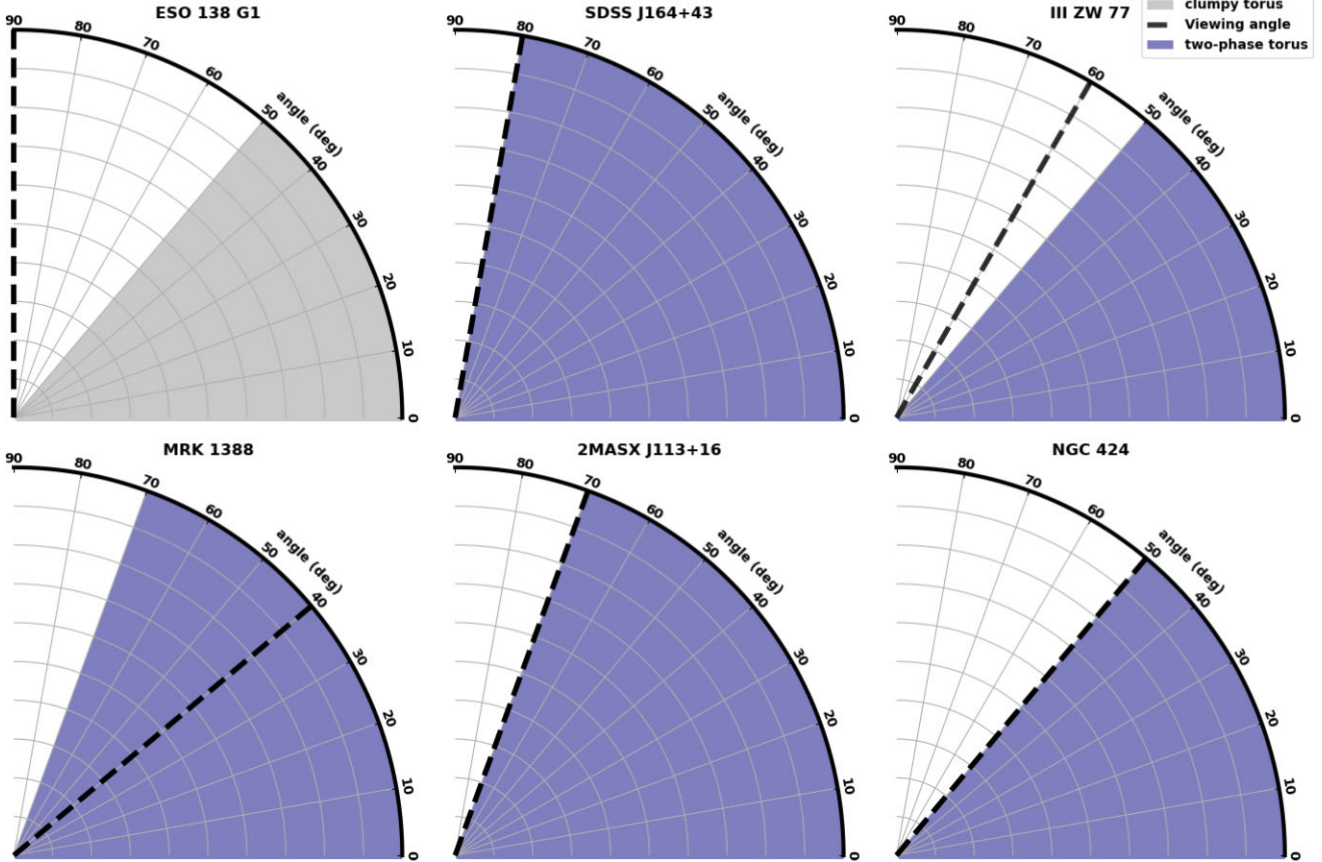


**Figure 12.** The representation of the parameters of the best fits. For fits made with CLUMPY, the grey area represents the half-opening angle of the clumpy torus ($\sigma$). For fits made with SKIRTOR, the half-opening angle of the two-phase torus ($\sigma$) is in purple. In all panels, the viewing angle ($i$) is represented by a black dashed line.

presence of dusty clouds in the line of sight. For the source best fitted with CLUMPY (ESO 138 G1), we found the presence of dust clouds in the polar region. We also found that in three objects of the sample (SDSS J164+4, 2MASX J113+16, and NGC 424), the fits made with SKIRTOR show that the viewing angle is such that, it coincides with the half-opening angle of the torus. This would explain the presence of broad components in the permitted lines, likely associate to the BLR, and an spectrum that overall looks like a Seyfert 2 in the optical.

Comparing the results obtained using CLUMPY and SKIRTOR, for CLiF and non-CLiF AGNs, we found that CLiF and non-CLiF AGNs behave similarly. This result shows that CLiFs cannot be treated as a separate class of AGNs. However, the number and intensity of CLs detected in the optical and NIR make CLiFs critical targets for understanding the processes behind the production of CLs, and the physical conditions of AGNs in general (see Prieto et al. 2022, for a recent study).

The number of CLiF AGNs classified as such up to today is small (seven in total). More objects with similar properties need to be identified in order to draw definitive conclusions about the nature of the CLR in CLiF AGN. The study of the known sample of such objects, in most cases, points out that they are compatible with Type I AGN orientation with significant influence of dusty clouds, favouring CL emission.

## DATA AVAILABILITY

Data products in the wavelength interval 1–2.5 microns will be shared on reasonable request to the corresponding author. Data employed in this work in the IR were downloaded from public databases of these facilities. The raw data products of the Spitzer spectra are available on the public Spitzer Heritage Archive at https://sha.ipac.caltech.edu/applications/Spitzer/SHA/. The photometric points from the space telescopes *WISE* and *AKARI* are available on the VizieR photometry tool at http://vizier.unistra.fr/vizier/sed/. Processed data products underlying this article will be shared on reasonable solicitation to the authors.

## REFERENCES

Alonso-Herrero A., Quillen A. C., Rieke G. H., Ivanov V. D., Efstathiou A., 2003, AJ, 126, 81
Antonucci R., Miller J., 1985, ApJ, 297, 621
Asmus D., 2019, MNRAS, 489, 2177
Asmus D., Hoenig S. F., Gandhi P., 2016, ApJ, 822, 109
Audibert A., Riffel R., Sales D. A., Pastoriza M. G., Ruschel-Dutra D., 2016, MNRAS, 464, 2139
Barvainis R., 1987, ApJ, 320, 537
van Bemmel I. M., Dullemond C., 2003, A&A, 404, 1
Braatz J., Wilson A., Gezari D., Varosi F., Beichman C., 1993, ApJ, 409, L5
Bruzual G., Charlot S., 2003, MNRAS, 344, 1000
Burtscher L. et al., 2013, A&A, 558, A149
Cameron M., Storey J. W., Rotaciuc V., Genzel R., Verstraete L., Drapatz S., Siebenmorgen R., Lee T. J., 1993, ApJ, 419, 136
Cerqueira-Campos F., Rodríguez-Ardila A., Riffel R., Marinello M., Prieto A., Dahmer-Hahn L., 2021, MNRAS, 500, 2666 (Paper I)
Chabrier G., 2003, PASP, 115, 763
Cid Fernandes R., Gu Q., Melnick J., Terlevich E., Terlevich R., Kunth D., Rodrigues Lacerda R., Joguet B., 2004, MNRAS, 355, 273
Cid Fernandes R., Mateus A., Sodré L., Stasińska G., Gomes J. M., 2005, MNRAS, 358, 363
Cokelaer T., Kravchenko A., Varma A., Brian Stringari C. E., Broda E., Pruesse E., msat59, , 2021, cokelaer/fitter: v1.4.0, available at: https://zenodo.org/record/5394791
Dahmer-Hahn L. G. et al., 2019, MNRAS, 482, 5211
Doi A., 2015, PASP, 67, 15
Edelson R., Malkan M., 1986, ApJ, 308, 59
Efstathiou A., Rowan-Robinson M., 1995, MNRAS, 273, 649
Elias J. H., Rodgers B., Joyce R. R., Lazo M., Doppmann G., Winge C., Rodríguez-Ardila A., 2006, in McLean I. S., Iye M., eds, Proc. SPIE Conf. Ser. Vol. 6269, Ground-based and Airborne Instrumentation for Astronomy. SPIE, Bellingham, p. 626914
Fritz J., Franceschini A., Hatziminaoglou E., 2006, MNRAS, 366, 767
García-Burillo S. et al., 2016, ApJL, 823, L12
García-Burillo S. et al., 2019, A&A, 632, A61
García-Burillo S. et al., 2021, A&A, 652, A98
Gelbord J. M., Mullaney J. R., Ward M. J., 2009, MNRAS, 397, 172
Girardi L., Bressan A., Bertelli G., Chiosi C., 2000, A&AS, 141, 371
Glidden A., Rose M., Elvis M., McDowell J., 2016, ApJ, 824, 34
González-Martín O. et al., 2019, ApJ, 884, 11 (GM19)
Granato G., Danese L., 1994, MNRAS, 268, 235
Gravity Collaboration, 2020, A&A, 634, A1
Hoenig S. F., Kishimoto M., Antonucci R., Marconi A., Prieto M. A., Tristram K., Weigelt G., 2012, ApJ, 755, 149
Hönig S. F., 2019, ApJ, 884, 171
Hönig S., Kishimoto M., 2010, A&A, 523, A27
Hönig S. F., Kishimoto M., 2017, ApJL, 838, L20
Hönig S. F. et al., 2013, ApJ, 771, 87
Hönig S. F., Watson D., Kishimoto M., Hjorth J., 2014, Nat., 515, 528
Kass R. E., Raftery A. E., 1995, J. Am. Stat. Assoc., 90, 773
Kishimoto M., Hönig S. F., Antonucci R., Millour F., Tristram K. R., Weigelt G., 2011, A&A, 536, A78
Krolik J., Kriss G., 1996, ApJ, 456, 909
Leftley J. H., Tristram K. R., Hönig S. F., Asmus D., Kishimoto M., Gandhi P., 2021, ApJ, 912, 96
Lira P., Videla L., Wu Y., Alonso-Herrero A., Alexander D. M., Ward M., 2013, ApJ, 764, 159
López-Gonzaga N., Burtscher L., Tristram K., Meisenheimer K., Schartmann M., 2016, A&A, 591, A47
Lopez-Rodriguez E. et al., 2018, ApJ, 859, 99
Martínez-Paredes M. et al., 2017, MNRAS, 468, 2
Müller-Sánchez F., Prieto M., Hicks E., Vives-Arias H., Davies R., Malkan M., Tacconi L., Genzel R., 2011, ApJ, 739, 69
Nandra K., George I., Mushotzky R., Turner T., Yaqoob T., 1997, ApJ, 477, 602
Nenkova M., Ivezić Ž., Elitzur M., 2002, ApJL, 570, L9
Nenkova M., Sirocky M. M., Ivezić Ž., Elitzur M., 2008a, ApJ, 685, 147
Nenkova M., Sirocky M. M., Nikutta R., Ivezić Ž., Elitzur M., 2008b, ApJ, 685, 160
Newville M., Stensitzki T., Allen D. B., Rawlik M., Ingargiola A., Nelson A., 2016, Astrophysics Source Code Library, record ascl:1606.014
Ochsenbein F., Bauer P., Marcout J., 2000, A&AS, 143, 23
Panda S., Czerny B., Adhikari T. P., Hryniewicz K., Wildy C., Kuraszkiewicz J., Śniegowska M., 2018, ApJ, 866, 115
Pier E. A., Krolik J. H., 1992, ApJ, 401, 99
Prieto A., Rodríguez-Ardila A., Panda S., Marinello M., 2022, MNRAS, 510, 1010
Rayner J., Toomey D., Onaka P., Denault A., Stahlberger W., Vacca W., Cushing M., Wang S., 2003, PASP, 115, 362
Rieke G., Lebofsky M., 1981, ApJ, 250, 87

Rieke G., Low F., 1975, Apj, 199, L13

Riffel R., Rodriguez-Ardila A., Pastoriza M. G., 2006, A&A, 457, 61

Riffel R. A., Storchi-Bergmann T., McGregor P. J., 2009, ApJ, 698, 1767

Riffel R. A., Bianchin M., Riffel R., Storchi-Bergmann T., Schönell A. J., Dahmer-Hahn L. G., Dametto N. Z., Diniz M. R., 2021, MNRAS, 503, 5161

Rose M., Elvis M., Tadhunter C. N., 2015a, MNRAS, 448, 2900

Rose M., Elvis M., Crenshaw M., Glidden A., 2015b, MNRAS: Lett., 451, L11

Schlawin E. et al., 2014, in Ramsay S. K., McLean I. S., Takami H., eds, Proc. SPIE Conf. Ser. Vol. 9147, Ground-based and Airborne Instrumentation for Astronomy V. SPIE, Bellingham, p. 91472H

Siebenmorgen R., Heymann F., Efstathiou A., 2015, A&A, 583, A120

Smith J.-D. T. et al., 2007, ApJ, 656, 770

Stalevski M., Fritz J., Baes M., Nakos T., Popović L. Č., 2012, MNRAS, 420, 2756

Stalevski M., Ricci C., Ueda Y., Lira P., Fritz J., Baes M., 2016, MNRAS, 458, 2288

Tristram K. et al., 2007, A&A, 474, 837

Tristram K. R., Burtscher L., Jaffe W., Meisenheimer K., Hönig S. F., Kishimoto M., Schartmann M., Weigelt G., 2014, A&A, 563, A82

This paper has been typeset from a TEX/LATEX file prepared by the author.